A machine learning framework for error compensation in radiative transfer calculations

Vijay B. Mohan Ramu*
Department of Mechanical and Aerospace Engineering, University of Kentucky, Lexington, KY, USA 40506

Amal Sahai†
AMA, Inc. at NASA Ames Research Center, Moffett Field, California 94035

Savio J. Poovathingal.‡
Department of Mechanical and Aerospace Engineering, University of Kentucky, Lexington, KY, USA 40506

Radiative heat transfer influences the amount of heat flux transferred to the surface of the hypersonic vehicle, which is essential to evaluate the performance of thermal protection systems. The radiative heat flux is found to be computationally prohibitive while accounting for the variation in spatial, angular, and spectral domains. A new methodology has been recently developed to alleviate the cost of computation in the spectral domain by constructing flow-agnostic reduced-order models (ROMs). The developed spectral ROM databases provide grouping strategies that account for non-equilibrium absorption and emission as well as interaction between disparate species due to spectral overlap in associated radiative processes. However, the developed ROMs need to be optimized for a specific combination of interacting gas species and would need to re-calibrated in case individual species are added/omitted. In this work, we use various machine learning (ML) techniques to approximate the radiative intensities determined by a ROM optimized for a specific gas mixture. The ML model relies on the ROM databases developed for a single species which ignores any spectral overlap. Thus, radiation evaluation starts with a simple summation of radiative intensities predicted using these non-calibrated ROMs for the contributing species. The ML framework then provides a correction to account for the interplay in the frequency, i.e., emission of photons by one species and absorption by another, and yields mixture-specific radiation fields. Once trained on the individual ROM databases, the ML framework offers instantaneous corrections that serves as a time/cost effective alternative to the optimization of ROMs for a specific gas mixture. The ML framework is trained on both the high fidelity and ROM evaluated line of sight (LOS) data from Orion, Stardust, and FIRE II cases to obtain a general purpose correction model for earth re-entry scenarios when radiation contributions from both atomic nitrogen and atomic oxygen are considered. A geometric length scale parameter is used in the training process to account for errors introduced in the ROM databases as a consequence of high optical thickness. The efficacy of the ML framework is underscored through extensive analysis of train and test errors with respect to all the re-entry scenarios. The applicability of such an ML framework was further corroborated by embedding it in a state-of-the-art US3D - NERO system for determining the radiative heat flux transferred to the hypersonic vehicle surface.

I. Nomenclature

RTE	=	Radiative transfer equation
$NERO$	=	Non-Equilibrium RadiatiOn
DOF	=	Degrees of freedom
LBL	=	Line-by-line

*Graduate Research Assistant, vbmo224@uky.edu.
†Research Scientist, Aerothermodynamics Branch, amal.sahai@nasa.gov
‡Assistant Professor, saviopoovathingal@uky.edu.

SVR	=	Support vector regression
PCA	=	Principal component analysis
SVM	=	Support vector machines
PVE	=	Proportion of variance
$RMSE$	=	RMSE
SVM	=	Support vector machines

II. Introduction

Atmospheric re-entry of spacecrafts offers significant design challenges owing to the various physical phenomena influencing the hypersonic flight. With an increasing need to design these vehicles to withstand the harsh atmospheres of far-off celestial bodies, the Mars Sample Return - Earth Entry Vehicle (MSR-EEV) [1] and Dragonfly [2], there is a need to reliably simulate thermo-chemical reactive flows, ablation, and radiation experienced at these extreme conditions. In addition, the physical phenomena affecting the re-entry vehicle must be evaluated in a coupled manner where the changes occurring as a consequence of these physical phenomena are reflected on the flow field surrounding the vehicle. This process is essential to ensure an efficient framework for vehicle design [3]. However, with respect to flow-radiation coupling, there are computational impediments to running state-of-the-art aerothermal analysis tools [4] and delivering efficient 3D spacecraft geometries within the relevant design cycle. Hence, it is necessary to relax the underlying system by employing simplifying assumptions or adopt other sophisticated techniques to deliver computationally tractable frameworks. In addition, there is a lack of a comprehensive overview of radiative heating and the interaction between radiation and flow field dynamics. This, in turn, leads to large safety factors in re-entry vehicle design. The state-of-the-art CFD solvers [5] have the ability to embed the radiation field originating from the thermochemically excited gas particles surrounding a re-entry vehicle. This embedding helps to model the energy transfer and the change in the thermochemical composition of the surrounding flow field as a result of radiation. The governing equation of such a radiation transfer process is given by Eq.1.

$$\mathbf{\Omega} \cdot \nabla I_\nu = J_\nu - \kappa_\nu I_\nu \tag{1}$$

In Eq. 1, I_ν is the monochromatic light intensity for a frequency ν in the direction Ω. J_ν and κ_ν are the emissivity and opacity corresponding to a particular frequency (ν). As represented, emissivity and opacity are functions of frequency and change drastically with a change in frequency. The opacity and emissivity at a particular frequency is obtained by adding contributions from all included radiative systems. The determination of total radiative intensity involves repeating calculations of the spectral intensity I_ν through the spatial domain for a fine spectral grid. Historically, the line-by-line approach (LBL) [6] and narrow-band models [7] have been used to resolve the spectral dimension of Eq. 1 by modeling the rapid changes in radiative coefficients with frequency. The use of such fine spectral discretization, usually composed of $O(10^5 - 10^6)$ distinct frequency points, allows both the heat transfer component and the induced thermochemical changes to be captured with exceptional accuracy. However, the cumulative cost of spatial-angular transfer evaluations, repeated for each frequency point, renders the analysis of large-scale problems unfeasible. In the recent past [8, 9], a novel reduced order modeling strategy has been conceived to spectrally resolve Eq. 1 over all the relevant frequencies. Built upon improving the applicability of Planck-averaging-based reduced-order spectral models for non-equilibrium gas mixtures [10, 11], the idea is to group the radiative coefficients such that an equivalent group emissivity (J_g) and a group opacity (κ_g) can be defined to represent a set of grouped frequencies. The group radiative coefficients can also be used to find the group radiative intensity (I_g). Hence, the total radiative intensity will be obtained by combining all of the group intensities. This ingenious solution helps to reduce the total number of calculations of Eq. 1 by several orders of magnitude and still reproduces the total spectral intensity with a loss of precision of only $\sim 5\%$. The verification and validation of such a spectral ROM database for different earth re-entry applications has been extensively covered by Sahai and Johnston [8, 9]. These ROM databases are constructed for either an individual species or a specific mixture of gasses without any knowledge from the flow simulations (a priori). Further, the flow field specific data is not used to construct the spectral ROM databases to prevent over-tuning of the frequency grouping strategy on a limited set of conditions. Although the ROM databases have been coupled to a CFD solver with well documented acceleration in the calculation of the surface radiative heat flux [9], there are limitations to the generalizability of this approach. A change in a single species contributing towards total radiative intensity would imply a complete re-calibration of the entire database for the following reasons. In addition, the thermochemically excited gas species in a mixture interact with each other by successive absorption and emission mechanisms, thereby jointly shaping the resulting value of frequency-dependent radiative coefficients. Hence, a novel spectral grouping strategy must be considered every time the radiation contribution of a given species that spectrally overlaps with the remaining species is considered or omitted. However, this is a tedious process and further poses challenges in the memory footprint/ease of evaluations of the ROM databases constructed for every possible combination of the gas species involved. An ML framework conceived to utilize the ROM databases constructed for individual species to model the mixture specific optimized ROMs serves as a time/cost effective alternative. The principal idea is to build extensive spectral ROM databases of individual species without the need to consider overlapping frequencies and using the summation of the individual contributions to approach towards an equivalent LBL solution. The ML framework conceived can be termed as a correction model as it is explicitly formulated to model the error between summation of individual ROM databases and its equivalent LBL solutions. In addition, the correction model will have the capability to model errors introduced in the ROM databases at high values of optical thickness. This is achieved by considering a geometrical length scale parameter (δs) as input parameter. Finally, in order to achieve the generalized ML framework for modeling the error in the radiative transfer calculation, several key objectives are met through this work.

- Determination of a closed form solution of an error term that corrects the total radiative intensities estimated by individual ROM databases to be closer to their LBL method equivalents.
- A robust correction framework that is generalized for multi species systems applicable to various re-entry applications.
- A framework that models the errors introduced in the ROM databases with change in optical thickness.
- Potential for reverse engineering the closed form solution obtained to infer the dependence of the error term on flow parameters.

In this work, we present the formulation, training, and validation of the ML correction model to achieve the specified objectives. The efficacy of such a correction model is further corroborated by embedding the model into a state-of-the-art flow field radiation coupled system (US3D - NERO) and comparing it to the optimized ROMs for a specific mixture. Several challenges plague the formulation of such a correction model, primary being the dimensionality of the underlying problem, which is large as a consequence of the number of parameters influencing the error term. These parameters include radiative intensity obtained from the summation of individual ROM databases, concentration of the involved species (atoms, molecules, ions, and electrons), flow conditions, and the geometric length scale parameter (δs). A common phenomenon in the development of ML models refers to the curse of dimensionality [12], which implies that an exponential increase in the training data is required to realize an ML model with increase in a single dimension. Hence, a principal component analysis (PCA) was initially performed to reduce the dimensionality of the underlying problem. The results of the PCA evaluations provided a new reduced set of input parameters which was later used for developing the closed form solution for the error term. PCA evaluations were chosen over Autoencoders [13] owing to its wide spread applications in the field of radiation [14–17]. A formulation of support vector regression (SVR) [18] formed the heart of the ML framework, as one of the main objectives was to obtain a closed form solution (surrogate model) for the correction term. Support vector regression was chosen over other available regression techniques due to its ability to handle problems with a moderate number of dimensionalities (~ 10) and its flexibility to employ kernel functions to suit the needs of the underlying problem [19]. In addition, kernel based techniques have found their use in modeling radiative coefficients as a function of various design parameters [20, 21] which further tipped the scales towards using SVR. The SVR framework resulted in an analytical solution that modeled the non-linear relationship between the correction term and the new parameters obtained from PCA evaluations. Finally, the PCA-SVR framework was coupled with the US3D-NERO system [8, 9] to correct radiative intensities and improve radiative transfer calculations. The current study is divided into four main sections: Sec. II provides the necessary background and articulates the objectives of the underlying problem. Section III expands on the problem statements and various techniques employed to realize the ML framework. Section IV starts with an explanation of the significance of the results obtained from the PCA evaluations, followed by the implementation of the ML framework. Section IV ends with a comprehensive performance evaluation of the underlying ML framework and its verification/validation through comparisons against the US3D-NERO [8, 9] system without the ML enhancements for a 3D Orion forebody. Section V summarizes the key objectives achieved and the scope of future work.

III. Methods

This section provides a more in-depth description of the steps used to meet the objectives of the current work. We start the section by clearly articulating the problem statement. Then, we describe the individual elements that constitute the ML framework and provide a detailed justification for our specific choices of the various tools employed.

A. Line-of-sight (LOS) analysis and data collection

In order to build an ML framework to model the correction term, we break down the 3D radiative field into a simple 1D LOS problem. Here, the 3D radiative field corresponds to the shock layer where a thermochemically excited gas particle emits photons that travel to the vehicular surface and contribute towards the surface radiative heat flux. LOSs that are normal to the vehicle surface were chosen to compute the radiative field. These LOSs were approximated as a 1D domain with a wall at one end and the provision to model the radiative energy generated throughout the domain as a consequence of emission and absorption of thermochemically excited gas particles. To further simplify the underlying problem, the radiative energy contributions from only atomic nitrogen and atomic oxygen were considered. Typically, the flow field in the shock layer of an earth re-entry vehicle consists of 11 species (N, $N+$, O, $O+$, NO, $NO+$, N_2, N_2+, O_2, O_2+ and $e-$) due to the dissociation and ionization of air at high temperatures (> 4000 K). However, a significant amount of radiative heating in the shock layer was found to be modeled through contributions from N and O [22] alone. Hence, we focus on radiative energy contributions from N and O for the current study, which serves as a proof of concept for future iterations of the framework where secondary contributions from other species will be considered. The 1D domain extracted from a hypothetical LOS is presented in Fig. 1.

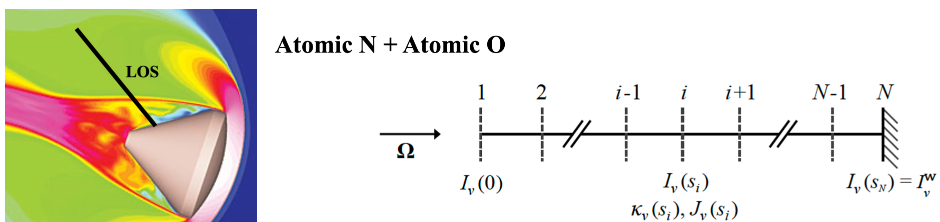

$$\frac{I_{LBL}}{I_{ROM}(N)+I_{ROM}(O)} = F_s$$

$$F_s = F_s(I_T^{ROM}(N) + I_T^{ROM}(O), M, \delta s, n_N + n_O, n_{N^+} + n_{O^+}, n_{e^-}, T, T_v)$$

Total spectral intensity ($I_T^{ROM}(s)$)	Molecular mass of the system (M)	Grid size (δs)	Number density of all photonic states ($n_N + n_O$)	Number density of ionized species ($n_{N^+} + n_{O^+}$)	Number density of free electrons (n_{e^-})	Translational-rotational temperature (T)	Vibrational – electronic temperature (T_v)

Fig. 1 Graphical representation of the problem statement and the data collection process required for training the ML framework.

The 1D domain is discretized into a set of pre-defined nodes. The radiative energy generated inside the domain undergoes successive absorption and emission throughout the domain, which in-turn changes the local spectral radiative intensity ($I_\nu(s_i)$) according to the governing Eq. 1. The total radiative intensity at each discretized node could be evaluated by resolving the frequency dependent radiation coefficients through the LBL method. As explained in Sec. II, the use of the LBL method to approximate the total radiative intensity becomes computationally intractable for a 3D radiative flow field. The ROM databases conceived to overcome this limitation exhibit a loss in accuracy (~ 5%) which grows with varying optical thickness (Δs) and further needs to be re-calibrated for every combination of gas species involved. Hence, the main goal of the current work is to come up with a framework that models the error term (F_s) at each discretized node of the domain to correct the radiative intensities given by the ROM databases (I_{ROM}) irrespective of the gas species/combination of gas species involved. The correction term at each node of the domain is defined by Eq. 2.

$$\frac{I_{\text{LBL}}}{I_{\text{ROM}}(N) + I_{\text{ROM}}(O)} = F_S \tag{2}$$

Note that Eq. 2 approximates the total radiative intensity of ROM to be a simple summation of individual contributions of N and O, respectively. In practice, this assumption is inaccurate as the grouping of frequencies in case of a multi species system should be dependent on each other as a consequence of overlapping frequencies. However, the following assumption serves the purpose of a close approximation to the LBL solution which can be corrected through the ML framework. The principal idea here is to build ROM databases of individual species, disregarding the problem of overlapping frequencies and using the summation of individual contributions to correct for the LBL solution. For example, let us consider a hypothetical case in which the radiation contributions from unknown species A, B, C, D and E. The ML framework would utilize individual ROM databases for each of the underlying species to correct for an LBL solution that involves any combination of the underlying species (3).

$$I_{\mathrm{LBL}} \simeq F_S \times [I_{\mathrm{ROM}}(A) + I_{\mathrm{ROM}}(B) + I_{\mathrm{ROM}}(C) + I_{\mathrm{ROM}}(D) + I_{\mathrm{ROM}}(E)] \tag{3}$$

This process of summing up individual ROM radiative contributions will be termed the "building block" model throughout this work. Essentially, we start off with "building block" approximations and train correction terms (F_s) to bridge the gap between the ROM approximations and the LBL solution. The ML framework, trained based on the above principles, would serve as a powerful tool that retains the acceleration of radiative transfer calculations as outlined in a previous study [8, 9] without the need for re-calibration with varying gas species or optical thickness.

We have outlined the basic principles that guide the training process of our ML framework. Next, we move onto the input parameters chosen to model the correction term. Several LOSs from hypersonic re-entry scenarios pertaining to Orion, Stardust, FIRE II and a meteor were considered for training the ML framework. Flow simulations for the above re-entry problems were performed using the non-equilibrium Navier Stokes solver [23]. A two temperature thermochemical model was used to resolve the thermal and chemical non-equilibrium effects at re-entry conditions [24]. The solved flow field was extracted from the simulations to perform radiative transfer calculations and determine the radiative heat flux. All flow parameters and species concentrations available from the simulations were chosen to model the correction term. In addition, the size of the grid (δs) and the molecular mass were added as additional input parameters to train the ML framework to be independent of the optical thickness and the type of gas species involved. This led to a situation where the correction term depended on 8 variables (Eq. 4).

$$F_s = F_s\Big(I_T^{\mathrm{ROM}}(N) + I_T^{\mathrm{ROM}}(O),\ M,\ \delta s,\ n_N + n_O,\ n_{N^+} + n_{O^+},\ n_{e^-},\ T,\ T_v\Big) \tag{4}$$

Equation 4 in conjunction with Eq. 2 formulates the underlying problem statement. The data required for training the ML framework were tabulated as represented in Fig. 1. As explained in Sec. II, every ML model suffers from a phenomenon known as the curse of dimensionality [12]. The need for a closed form solution to F_s and the known problem of regression type ML models in handling a large volume of data (> 10000 training points) enabled us to look for sophisticated feature extraction techniques. One such technique used in the current work, known as principal component analysis, will be explained in the next section.

B. Principal component analysis (PCA) and feature extraction

Feature extraction is a core step in data pre-processing that transforms raw, high-dimensional observations into a more compact and informative representation. The goal is to isolate the most relevant characteristics of the data while reducing redundancy, noise, and computational cost. Effective feature extraction improves the performance of downstream machine-learning tasks such as, classification, clustering, and regression by enhancing class separability and reducing the dimensionality burden that often leads to overfitting [25]. Given a data set:

$$X = \{\mathbf{x}_1, \mathbf{x}_2, \ldots, \mathbf{x}_n\}, \qquad \mathbf{x}_i \in \mathbb{R}^d \tag{5}$$

the goal is to learn a mapping:

$$\Phi : \mathbb{R}^d \to \mathbb{R}^k, \qquad k < d, \tag{6}$$

such that the low-dimensional feature

$$\mathbf{z}_i = \Phi(\mathbf{x}_i) \tag{7}$$

captures the most informative structure in the data while reducing redundancy, noise, and computational burden [25]. This is typically formulated as an optimization problem:

$$\Phi^* = \arg\max_{\Phi} J(\Phi(X)), \tag{8}$$

where $J(\cdot)$ is a criterion measuring the informativeness of transformed features (e.g., variance, mutual information, or class separability).

Among the most widely used linear feature-extraction techniques is Principal Component Analysis (PCA), a statistical method that constructs new orthogonal variables called principal components (PCs) by projecting data onto directions of maximum variance. PCA identifies latent structure in high-dimensional datasets and provides an optimal linear transformation in the sense of minimizing the reconstruction error under a norm l_2 [26]. Because PCA is unsupervised, it is particularly useful in exploratory data analysis, noise filtering, visualization, and initialization of other machine-learning models [27]. Assuming centered data, the covariance matrix is:

$$\mathbf{C} = \frac{1}{n}\mathbf{X}^{\top}\mathbf{X}, \tag{9}$$

PCA solves the eigenvalue problem:

$$\mathbf{C}\mathbf{w} = \lambda\mathbf{w}, \tag{10}$$

where λ represents the variance captured along the direction $\mathbf{w}$. Let the eigenvalues be ordered as:

$$\lambda_1 \geq \lambda_2 \geq \cdots \geq \lambda_d. \tag{11}$$

Then the projection matrix for the top-k principal components is:

$$\mathbf{W}_k = [\mathbf{w}_1 \ \mathbf{w}_2 \ \cdots \ \mathbf{w}_k]. \tag{12}$$

Each sample is then transformed as:

$$\mathbf{z}_i = \mathbf{W}_k^{\top}\mathbf{x}_i. \tag{13}$$

For our application, the correction term (F_s) is assumed to be dependent on 8 variables ($I_T^{\mathrm{ROM}}(N)+I_T^{\mathrm{ROM}}(O)$, M, δs, $n_N + n_O$, $n_{N^+} + n_{O^+}$, n_{e^-}, T, T_v). Our goal is to employ PCA to reduce the dimensionality of F_s as explained through Eqs. 5 - 13. In Eq. 5, X is a matrix of dimension $N \times 8$ containing the training data. Hence, each $\mathbf{x_i}$ is a vector of 8 input parameters that correspond to a particular value of F_s. The PCA formulation finds a set of new orthogonal axes ($\mathbf{W_k}$), where each orthogonal component ($\mathbf{w_i}$) is a linear combination of the 8 original input parameters. In Eq. 13, each instance of F_s corresponding to a data point $\mathbf{x_i}$ will be transformed to the new space of orthogonal components given by Eq. 14. As the principal components that define the new orthogonal space (k) are less than the original space ($d = 8$), a reduction in dimensionality is achieved.

$$Z = \{\mathbf{z}_1, \mathbf{z}_2, \ldots, \mathbf{z}_n\}, \qquad \mathbf{z}_i \in \mathbb{R}^k \tag{14}$$

The main principal components chosen to form Z in Eq. 14 depend on the percentage of variance embedded in each orthogonal component ($\mathbf{w_i}$), given by the eigenvalue corresponding to each $\mathbf{w_i}$. From this point of view, the formulation of PCA can be explained as finding a new space that maximizes the variance of the initial data set:

$$\mathbf{W}_k = \arg\max_{\mathbf{W}^{\top}\mathbf{W}=\mathbf{I}_k} \mathrm{Tr}(\mathbf{W}^{\top}\mathbf{C}\mathbf{W}). \tag{15}$$

By re-arranging the principal components based on their eigenvalues and choosing the dominant eigenvectors, the reconstruction error in Z when compared to X can be minimized. Alternatively, PCA can also be explained as a technique that finds a reduced orthogonal space that minimizes the l_2 norm associated with $\mathbf{z_i}$, given by Eq. 16:

$$\mathbf{W}_k = \arg\min_{\mathbf{W}^{\top}\mathbf{W}=\mathbf{I}_k} \sum_{i=1}^{n} \|\mathbf{x}_i - \mathbf{z_i}\|_2^2, \tag{16}$$

Theoretically, it is possible to completely re-construct the original data by using all the principal components ($\mathbf{W_k}$) obtained from Eq. 15. However, this does not produce a reduction in the dimensionality of the problem. Hence, it is necessary to pick the principal components that minimize the reconstruction error (Eq. 16). The process adopted to choose the principal components and the resulting new reduced orthogonal space will be explained in detail in Sec. IV. Next, we look at the regression model adopted to capture the non-linear relationship between F_s and the new parameters obtained from PCA evaluations.

C. Support vector regression (SVR)

In our current study, we employ a robust and flexible regression technique based on support vector machines (SVM), called support vector regression (SVR), first identified by Vapnik et al. in 1992 [18, 28, 29]. One of the main advantages of SVR over its counterparts is its ability to approximate random noise in the sampling data. Conventional regression techniques are normally hindered by a limited number of frequencies and the kernel function chosen for approximating the data points. Most real life engineering problems including our current problem statement are multi modal in nature with complex correlations between the input parameters. This requires a more involved regression technique such as SVR and is considered a necessity when the dimensionality of the problem increases.

SVR is a non-parametric technique because it relies on kernel functions. The goal is to find a function $f(x)$ that deviates from y_n (training data value) by a value no greater than a loss parameter (ϵ) for each training point x_i, and at the same time is as flat as possible. Even with the introduction of ϵ as the loss parameter, there can be cases where there is no function $f(x)$ that solves the loss minimization problem. In order to overcome this limitation, SVR introduces an additional parameter called slack variable, which acts as a soft margin. SVR reduces the problem statement to obtaining a set of dual co-efficients $(\alpha - \alpha^*)$ and support vectors (x_i) that are estimated by solving a minimization problem shown in Eq. 17, which is constrained by Eqs. 18 and 19. A universal intercept is determined for all support vectors according to a second minimization problem shown in Eq. 20 constrained by Eqn. 21 such that the approximations are always bounded by the soft margin, the slack variable (ζ). Q_{ij} in Eq. 17 is an $n \times n$ positive semi-definite matrix consisting of kernel functions $(G(x_i)^T G(x_j))$, y^T is the output vector associated with each training data and e is a vector of ones which facilitates the summation of slack variable defined for every training point. The dual minimization problem is setup to reduce the error associated with the introduction of slack variables.

$$min\left[\frac{1}{2}(\alpha - \alpha*)^T Q(\alpha - \alpha^*) + \epsilon e^T(\alpha + \alpha^*) - y^T(\alpha - \alpha^*)\right] \tag{17}$$

subject to

$$\left[e^T(\alpha - \alpha^*) = 0\right] \tag{18}$$

$$\left[0 \leq \alpha_i, \alpha_i^* \leq C, i = 1, 2, ..., n\right] \tag{19}$$

$$min\left[\|y_i - G(x_i) - b\| \leq \|\epsilon + \zeta_i\|\right] \tag{20}$$

subject to

$$\zeta_i \geq 0, i = 1, 2, ...n \tag{21}$$

The hyper-parameters, ϵ, ζ, and C must be tuned to best suit the objectives of a given application. In SVR, the regularization parameter (C) influences the rigidity of the surrogate model. In the current work, C is optimized using a trial-and-error approach to meet the objectives. The trained model is then validated against the test data generated beyond the scope of the sampling data to ensure that the model does not suffer from over-fitting. The validation process with the respective graphs will be covered in greater detail in the results section (Sec. IV). The other hyper-parameters are also obtained through a trial and error approach to determine the best values for the hyper-parameters that lead to a maximum relative error of 8% in the training data points.

Once the dual minimization problem is solved (Eqs. 17-21), an analytical function can be constructed for the chosen kernel function, which relates the input variables with its corresponding output. The predictive function after implementing SVR on a set of training vectors is given by Eqn. 22.

$$f(x) = \Sigma_i^n(\alpha_i - \alpha_i^*)G(x_i, x) + b \tag{22}$$

where x_i is the support vector obtained from training, n is the number of support vectors, $(\alpha_i - \alpha_i^*)$ are the dual coefficients, x is the input vector, $G(x_i, x)$ is the kernel function and b is the intercept. In this work, a Gaussian function (Eq. 23) is used as the kernel function (G) to approximate the random errors associated with the stochastic process.

$$G = \exp(-\gamma\|x_i - x\|^2) \tag{23}$$

In Eq. 23, γ is an extra hyper-parameter associated with the regression problem when radial basis functions such as a Gaussian function are used as the kernel. The hyper-parameter γ defines the influence of each training point on the overall error while the term $||x_i - x||^2$ computes the error of each training point with respect to the support vectors. In the present study, the above SVR formulation will be used to develop a non-linear relationship between F_s and the new orthogonal space obtained after the PCA evaluations. The non-linear relationship will be of the form described by Eq. 22. Using the support vectors, dual coefficients and the intercept obtained from the SVR formulation, Eq. 22 can be evaluated at every discretized point of the 3D radiative flow field to correct the radiative intensity of ROMs. The complete implementation of SVR and a comprehensive evaluation of its performance will be presented in Sec. IV.

D. ML model coupled to US3D-NERO framework

The principal deliverable of the present work is an ML model that corrects the radiative intensities predicted by the radiation solver, titled Non-Equilibrium RadiatiOn (NERO). NERO incorporates finite volume spatial discretization, mesh reordering, Lebedev-type quadrature, and reduced-order spectral models that are linked with existing NASA aero-thermal analysis software [8, 9]. The object oriented based nature of NERO is leveraged to embed the ML model into the radiative solver with ease (Fig. 2). NERO runs in conjunction with US3D [5], one of NASA's workhorse CFD tools, to compute radiative heat flux and radiation-induced energy/mass source terms for the flow field. The US3D finite-volume flow code solves the chemically reacting non-equilibrium Navier-Stokes equations on unstructured grids. The ML model developed in this work is embedded in NERO as represented in Fig. 2, to improve the capabilities of the US3D-NERO framework.

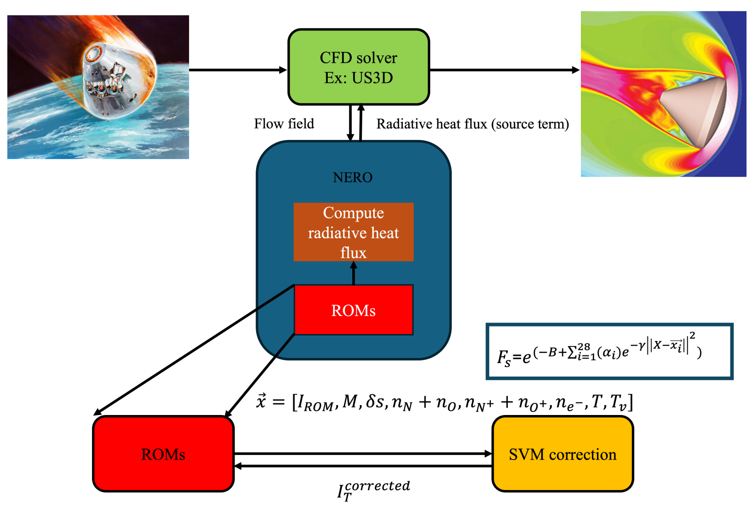

Fig. 2 Graphical representation of implementation of the correction model to the state-of-the-art US3D-NERO framework.

Consider a specific point in the trajectory of a re-entry vehicle about to enter the earths atmosphere. A trajectory point is generally defined by the speed and altitude of the vehicle. The chemically reactive non-equilibrium flow surrounding the re-entry vehicle is first solved by US3D. The flow field at this trajectory point is extracted using the radiation solver toolbox (NERO) to calculate the radiative heat flux using the spectral ROM database (Sec. II). The radiation intensities predicted by the ROM database for individual species (building block model) are corrected by the ML model to obtain a solution closer to the ROM database optimized for a specific mixture (N and O). The computations required to achieve this correction are as follows. First, the radiative intensity predicted by the ROM database and the flow conditions extracted from US3D are used to construct the input vector (**x**) at each point of the discretized 3D radiative field. Next, all the elements of the input vector are logarithmically scaled and normalized with respect to physical constants. The normalized vector is then projected onto the orthogonal space obtained from the PCA evaluations. Finally, Eq. 22 operates in the new orthogonal space to predict the correction terms at each point of the discretized 3D radiative field. Equation 2 makes use of the correction term predicted by the ML model to obtain a radiative flux closer to the optimized ROM database for a specific mixture. The new radiative flux is used as a source term in the governing equations of the US3D solver to speed up the 2-way coupling between the CFD and radiative solver (NERO). One of the main advantages of the US3D-NERO system over legacy tools such as the LAURA-HAURA system [23] is its ability to predict the surface heat flux and the 3D radiative field with significantly less computational resources [8, 9]. In Sec. IV, the above coupling method will be verified by comparing the ability of an ML enhanced US3D-NERO system against optimized ROMs of O and N radiation to predict the surface heat flux experienced by the Orion space capsule.

IV. Results

A total of three hypersonic re-entry scenarios and their accompanying radiative field as a consequence of atomic nitrogen and atomic oxygen are considered to generate the training data. These scenarios include: 1) the Orion capsule, 2) a FIRE II experiment, 3) the Stardust probe. Flow simulations for these scenarios have been performed using the LAURA non-equilibrium Navier-Stokes solver [23]. The non-equilibrium dynamics of the gaseous mixture is described using a two-temperature thermochemical model comprising 11-species (N, $N+$, O, $O+$, NO, $NO+$, N_2, N_2+, O_2, O_2+ and $e-$) and kinetic rates presented by Johnston and Panesi [24]. The freestream conditions for each of the three cases under study along with references detailing the computational setup are:

- Orion capsule analyzed under free stream conditions of V_∞ = 10.5 km/s, ρ_∞ = 2.73 × 10^{-4} kg/m^3 and T_∞ = 244 K, which corresponds to peak heating lunar-return conditions [30].
- Stardust entry analyzed at the 46 s trajectory point, corresponding to a free stream velocity of 11.69 km/s and a free stream density of 1.05 × 10^{-4} kg/m^3 [31].
- FIRE II entry analyzed at the 1636 s trajectory point, corresponding to a free stream velocity of 11.31 km/s and a free stream density of 8.57 × 10^{-5} kg/m^3 [32].

Once the non-equilibrium flows surrounding the vehicles/bodies are resolved, LOSs along the forebody stagnation line and through the wake (starting from the backshell) are extracted for training the ML model. Specifically, the LOSs extracted to train the model are represented in Table 2.

Table 2 LOSs pertaining to the hypersonic re-entry scenarios used for training the ML model.

No.	Training set	Grid amplification factor (Δs)
1	Orion stagnation LOS	1,25,50
2	FIRE II stagnation LOS	1,25,50
3	FIRE II wake LOS	1,25,50
4	Stardust stagnation LOS	1,25,50
5	Stardust wake LOS	1,25,50

To address one of the main goals of the current work, the optical thicknesses of the considered LOSs for training are changed using the grid amplification factor to obtain ML corrections that can accommodate a wider range of radiative scenarios. For example, with the use of amplification factors (Δs) of values 1, 25, and 50, different stagnation LOSs of the Orion capsule with varying optical thicknesses can be included in the training data. The idea is to capture the effects of varying optical thickness with the help of the geometric length scale parameter (δs) included as one of the input variables. Each discretized point of all the LOSs represented in Table 2 is considered a data point for training. Hence, the training data are tabulated as in Fig. 1 to form a matrix $N \times 8$, where N refers to the total number of training data and the number "8" refers to the total number of input variables considered. In this work, N is associated with a total number of ~ 5000 training points. The correction term (F_s) corresponding to each training vector (each row of $N \times 8$ matrix) is calculated according to Eq. 2, where F_s models the error between fully resolved LBL radiative intensities and the "building block" estimation of total radiative intensity. Here, the "building block" refers to a simple summation of ROM databases independently calibrated for atomic nitrogen and atomic oxygen. In addition, the training data set is logarithmically scaled and normalized with respect to the physical constants. Normalization and scaling help PCA to effectively isolate the orthogonal components and perform a reduction in the dimensionality. In this work, all input variables are normalized with respect to physical constants to make the trained model independent of the range of training data.

A. Significance of PCA evaluations

Consider the underlying PCA problem statement, where the scaled and normalized training data (X: a matrix of dimensions $N \times 8$) must be compressed into an orthogonal space of lower dimensions. The new orthogonal space is defined by solving an eigenvalue problem with respect to the co-variance matrix (C) of the initial data set (X). The set of eigenvectors ($\mathbf{W}_8 = [\mathbf{w}_1\ \mathbf{w}_2\ \cdots\ \mathbf{w}_8]$) obtained after solving Eq. 15 represents the new orthogonal space, where each eigenvector is a linear combination of initial "8" input variables ($I_T^{\mathrm{ROM}}(N) + I_T^{\mathrm{ROM}}(O), M, \delta s, n_N + n_O, n_{N^+} + n_{O^+}, n_{e^-}, T, T_v$). As explained in Sec. III.B, the goal of the PCA is to find the orthogonal space that maximizes the variance present in the initial data set while minimizing the l_2 norm associated with the projection onto the new orthogonal space (Eq. 16). A measure of the total variance and therefore the reconstruction error is obtained by computing the proportion of variance (PVE) with respect to each eigenvector and using the corresponding eigenvalue (Eq. 24).

$$\mathrm{PVE}_i = \frac{\lambda_i}{\sum_{j=1}^{d} \lambda_j} \tag{24}$$

In Eq. 24, the eigenvalue (λ_i) associated with each eigenvector is compared with the sum of all eigenvalues ($\sum_{j=1}^{d} \lambda_j$) to obtain the PVE of a particular eigenvector. It is also possible to compute the cumulative PVE by considering contributions from multiple eigenvectors in the numerator of Eq. 24. Both PVE and cumulative PVE point towards the variance captured/retained by using a particular eigenvector or a set of eigenvectors representing the new orthogonal space. For example, a PVE value of 0.8 (80%) associated with any single eigenvector implies that projection of the initial data set onto the orthogonal space ($\mathbf{z}_i = \mathbf{W}^\top \mathbf{x}_i$) reproduces the original data with 80% accuracy. This PVE data with respect to the dominant eigenvector (largest value of PVE) obtained for a series of PCA evaluations performed on different training data sets are given by Table 3.

Table 3 Convergence of the principal eigenvector across different training sets and corresponding variance reproduced.

Training sets	Dominant eigenvector	PVE
1,2,3,4,5	[−0.017, −0.0977, −0.98, −0.026, −0.093, −0.031, −0.0317, −0.033]	80%
2,3,4,5	[−0.031, −0.099, −0.97, −0.058, −0.162, −0.066, −0.048, −0.051]	85%
1,3,4,5	[0.012, 0.099, 0.99, 0.029, 0.097, 0.029, 0.029, 0.031]	86%
1,2,3,5	[0.017, 0.096, 0.988, 0.028, 0.097, 0.033, 0.033, 0.035]	77%
1,2,4,5	[0.043, 0.094, 0.989, 0.017, 0.073, 0.036, 0.038, 0.039]	75%
1,2,3,4	[0.049, 0.090, 0.987, 0.015, 0.070, 0.031, 0.035, 0.033]	79%

The first column of Table 3 represents the set of LOSs used to perform the PCA analysis. The numbering methodology is consistent with the LOSs represented in Table 2. The second column represents the dominant eigenvector obtained for each PCA evaluation and the third column represents the corresponding PVE value. From Table 3, we can see that the dominant eigenvector holds > 75% of the variance for all permutations of PCA evaluations performed. Furthermore, the components of the dominant eigenvector are nearly identical. This implies a situation where the PCA evaluations converge to the same dominant eigenvector when the training data is varied. This is a powerful solution as it underscores the potential of PCA to obtain a principal direction that maximizes variance. For our application, the new orthogonal space is chosen to be defined by the dominant eigenvector (Table 3). As explained in Sec. III.B, the choice of eigenvectors that define the orthogonal space is a trade off between the precision of the projected data and the resulting reduction in dimensionality. Since our purpose is to train a regression model that operates in the new orthogonal space, we perform a trial and error approach to choose the appropriate set of eigenvectors. Multiple regression models were developed using 1,2,... up to a full set of 8 eigenvectors, and the performance of the resulting ML models was evaluated. No visible improvement in the performance of the ML model was inferred from the use of more eigenvectors in addition to the dominant eigenvector (Table 3). Hence, the new orthogonal space obtained from the PCA evaluations was chosen to be represented only by the dominant eigenvector. This resulted in a significant reduction in the dimensionality of our problem statement, from 8 dimensions to a single dimension.

It should be noted that the new orthogonal space obtained from the PCA evaluations is directly dependent on all initial variables, as the dominant eigenvector is a linear combination of the 8 initial variables ($I_T^{\mathrm{ROM}}(N) + I_T^{\mathrm{ROM}}(O), M, \delta s, n_N + n_O, n_{N^+} + n_{O^+}, n_{e^-}, T, T_v$). The data compression obtained from the PCA transformation can be explained as follows. Let us assume that there exists a scaled and normalized training vector $\mathbf{x_i}$ whose components are given by $(x_1, x_2, x_3, ..., x_8)$ respectively. A projection of $\mathbf{x_i}$ onto the new orthogonal space implies a vector transformation $W^T x_i$, where W^t represents the dominant eigenvector. The resulting transformation is a scalar value (z) which is equivalent to the vector $\mathbf{x_i}$ in the initial higher dimensional space. This transformation can be performed for all training vectors, helping to represent the $N \times 8$ training matrix as a vector of N elements in the new orthogonal space. Hence, achieving a compression factor of 8. The compression and linearization performed by the PCA helps the regression model to effectively capture the correction terms with the least amount of training points.

B. ML model to predict the correction terms

PCA converts the underlying 8 dimensional problem statement into a single dimension as represented by Eq. 25. In Eq. 25, z is a scalar given by a vector transformation of the training vector $x_i = (I_T^{\text{ROM}}(N) + I_T^{\text{ROM}}(O), M, \delta s, n_N + n_O, n_{N^+} + n_{O^+}, n_{e^-}, T, T_v)$ into the new reduced space, defined by the dominant eigenvector (Table 3). Hence, the correction term (F_s) now depends on the scalar z. This significantly simplifies the underlying regression problem and helps SVR to effectively model the changes of F_s with the scalar z.

$$F_s = F_s\Big(I_T^{\text{ROM}}(N) + I_T^{\text{ROM}}(O),\ M,\ \delta s,\ n_N + n_O,\ n_{N^+} + n_{O^+},\ n_{e^-},\ T,\ T_v\Big) --> F_S = F_S(z) \tag{25}$$

Furthermore, dimensionality reduction is necessary because there is no user control over the data sampling process. In other words, sophisticated techniques like Latin hypercube sampling (LHS) [33] cannot be employed to populate the original 8 dimensional domain. The available data are directly lined to the LOSs extracted from the flow fields surrounding the hypersonic re-entry scenarios (Table 2). Hence, it is necessary to carefully choose the data set that captures maximum variance without redundancy. This is achieved through the application of PCA, which extracts the features required to effectively represent the randomly chosen training data set. Once PCA is performed, the training vectors are converted into their respective scalars, and SVR is primed to model the relationship between F_s and z. Such an SVR formulation is carried out according to the procedure explained in Sec. III.C and the resulting solution is given by Eq. 26.

$$F_s(z) = \exp\left[-0.0966 + \sum_{i=1}^{28} (\alpha_i - \alpha_i^*) \exp(-1.32\|z_i - z\|^2)\right] \tag{26}$$

Equation. 26 is identical to the form given by Eq. 22. A term by term comparison reveals the values for intercept (b), hyper-parameter γ, number of support vectors (z_i), and dual coefficients ($\alpha_i - \alpha_i^*$) associated with each support vector. The support vectors are just scalars because of the 1D regression problem solved in this work. The visible hyper-parameter γ and the invisible hyper-parameters (C and ζ) directly control the performance of the ML model.

The initial set of values assumed for the hyper-parameters (γ, C and ζ) are optimized with respect to the l_2 corresponding to the training data. The ML model resulting from the l_2 norm based method can lead to higher prediction error on unseen data. Furthermore, specific situations may arise where the maximum error associated with the model can occur at specific points of interest. For example, in our application, it is necessary to obtain good predictions at the wall of the 1D domain (Fig. 1), as it corresponds to the total radiative intensity transferred to the surface of the hypersonic vehicle, which is an important design parameter for developing thermal protection systems. The l_2 norm method can result in an ML model in which high errors are associated with the prediction of radiative intensities at the wall even though errors are minimized across the entire domain. This is an undesirable solution. Hence, we employ a user defined objective function to optimize the hyper-parameters, which results in an ML model that has good predictions at the wall, strictly bound maximum error and a low root mean square error (RMSE) across the domain.

$$Objective\ function = w_1 \times RMSE + w_2 \times Max(err) + w_3 \times err_{wall} \tag{27}$$

In Eq. 27, the weights (w_1,w_2, and w_3) are user defined and decided on a trial and error approach with respect to the performance of the model exhibited across unseen data. An in-house modified version of the popular GridSearchCV algorithm [34] is used to optimize the hyper-parameters for the user defined objective function (Eq. 27). The final SVR solution (Eq. 26) obtained after the hyper-parameter optimization process can be used to predict the correction term (F_s) associated with all discretized points in a 3D radiative field. The process of obtaining the predictions F_s is as follows. A prediction vector is first constructed as $\mathbf{x_i} = (I_T^{\text{ROM}}(N) + I_T^{\text{ROM}}(O), M, \delta s, n_N + n_O, n_{N^+} + n_{O^+}, n_{e^-}, T, T_v)$ by noting the values of all input variables at a certain discretized point. $\mathbf{x_i}$ is then logarithmically scaled and normalized according to the chosen physical constants. This is followed by projection of $\mathbf{x_i}$ onto the 1D reduced space ($z = \mathbf{W^T x_i}$), defined by the dominant eigenvector (Table 3). The resulting scalar z is plugged directly into Eq. 26 to obtain F_s corresponding to the prediction vector $\mathbf{x_i}$. Finally, Eq. 2 uses the predicted F_s to correct the radiative intensity associated with the given discretized point.

C. Error analysis

Over-fit and under-fit conditions represent the common pitfalls experienced by any ML model as a consequence of sampling scheme, clustering of training data, and choice of hyper-parameters adopted to train the underlying model. The sensitivity of the trained framework to over-fit and under-fit conditions can be verified by performing extensive error analysis on the training and test data. For our current application, the error of predictive radiative intensity with respect to LBL resolved radiative intensity provides valuable information about the performance of the regression model and its tendency to exhibit over-fit/under-fit conditions. The relative error for all training and test points was calculated with respect to the LBL resolved radiative intensity and given by Eq. 28 and Eq. 29.

$$\%\,\mathrm{error(SVM)} = \frac{\left\| I_T^{\mathrm{SVM}} - I_T^{\mathrm{LBL}} \right\|}{I_T^{\mathrm{LBL}}} \times 100 \tag{28}$$

$$\%\,\mathrm{error(ROM)} = \frac{\left\| I_T^{\mathrm{ROM}} - I_T^{\mathrm{LBL}} \right\|}{I_T^{\mathrm{LBL}}} \times 100 \tag{29}$$

In both Eqs. 28 and 29, I_T^{LBL} corresponds to the fully resolved total radiative intensity at each point of the discretized domain (Fig. 1), I_T^{SVM} corresponds to the total radiative intensity obtained by correction through the ML Model,and I_T^{ROM} corresponds to the total radiative intensity estimated by both the "building block" model and the ROM databases calibrated for case specific application. The performance of the ML model on the training data can be verified by evaluating the relative errors (Eqs. 28 and 29) in the LOSs used for training. The plotted parameters and the color scheme used in Fig. 3 are identical to all the plots that succeed. Hence, Fig. 3 will be used as a reference to articulate all the plotted parameters.

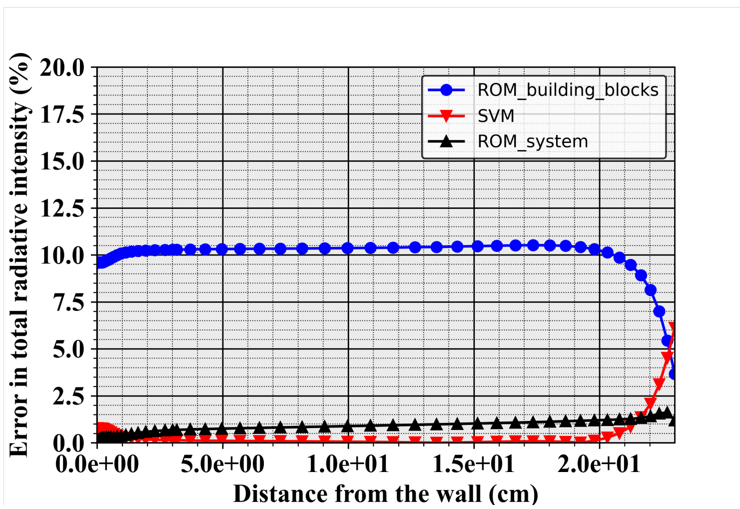

Fig. 3 Variation of relative error in Orion stagnation LOS.

Figure 3 represents the variation of relative errors compared to the fully resolved total radiative intensity in the stagnation LOS of the Orion capsule. The "ROM building blocks" curve (blue coded) represents the initial approximation of the total radiative intensity before the ML correction. As explained in Sec. III.A, the "building blocks" model assumes that the total radiation contribution of a system containing atomic nitrogen and atomic oxygen is a simple summation of its respective ROM radiative intensities ($I_T^{ROM} = I_T^{\mathrm{ROM}}(N) + I_T^{\mathrm{ROM}}(O)$). As represented in Fig. 3 the relative error associated with respect to the "building block" model is high. This behavior can be explained by the fact that the grouping strategy of the radiative coefficients used by the ROMs is dependent only on individual species without any accommodations for the interactions between the involved species. In other words, in a radiative field consisting of contributions from multiple species, the photons emitted by one species are absorbed by the other species which adds further complexities in the handling of radiation coefficients dependent on overlapping frequencies. The grouping strategy employed to accelerate the radiative transfer calculation accounts for the overlapping frequencies of emission and absorption mechanisms while the solution of RTE for the combined radiation coefficients of all the involved species accounts for the interaction between the species. This approach necessitates the re-calibration of the ROM database for every mixture specific case. Such a mixture specific calibration of the ROM database for the application of stagnation LOS of Orion is represented by "ROM system" curve (black coded) in Fig. 3. Note the considerable reduction in the relative error associated with "ROM system" when compared to "ROM building block". The mixture specific grouping of ROM (ROM system) is a tedious and time consuming practice that must be repeated with the addition of every gas species. In this work, we augment the independently developed ROM database (ROM building blocks) by modeling its error with respect to the fully resolved solution. The modeled error through the ML framework will be used to obtain the new total radiative intensity represented by the "SVM correction" curve (red coded) in Fig. 3. Note the considerable reduction in relative error associated with the "SVM correction" compared to the "ROM building block" and its close proximity to the "ROM system", in Fig. 3. In simple words, the "SVM correction" curve (red coded) uses the "building block" curve (blue coded) as an initial approximation to provide a solution closer to the "ROM system" curve (black curve). Similar behavior to Fig. 3 was observed in all the LOSs used for data sampling (Figs. 4(a) - 4(d)).

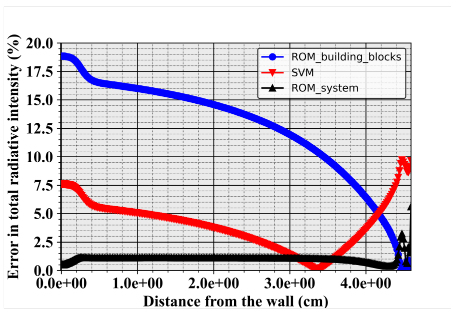

(a) Variation of relative error in FIRE II stagnation LOS.

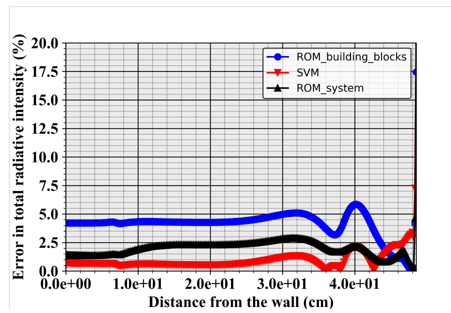

(b) Variation of relative error in FIRE II wake LOS.

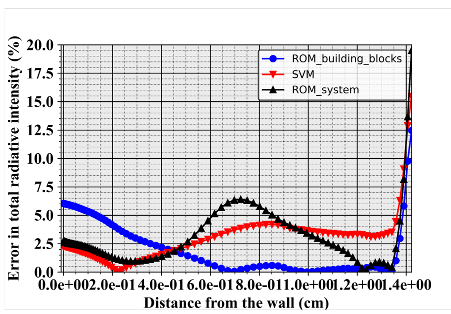

(c) Variation of relative error in Stardust stagnation LOS

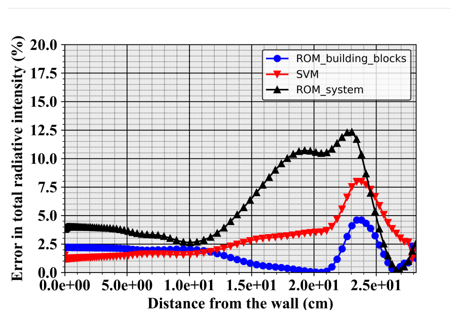

(d) Variation of relative error in Stardust wake LOS

Fig. 4 Variation of relative error in LOSs used for data sampling.

Note that in Figs. 4(a) - 4(d), the ML corrected radiative intensities (red curve) have considerably lower relative error when compared to the "building block" model (blue curve). In addition, the ML corrected predictions are closer to the "ROM system" curves (black coded), sometimes even better than the case specific calibrated ROMs. Figure 3 in conjunction with Fig. 4 verifies the ability of the ML model to correct the radiative intensities in LOSs used as training data. Hence, the ML model is shown to be indifferent towards the under-fit condition.

Next, we look at LOSs that are unseen by the ML model and verify its performance across these LOSs. A total of 21 LOSs surrounding the Orion capsule during a re-entry scenario were extracted as represented by Fig. 5(a). The average radiative intensity across these LOSs were plotted (Fig. 4(b)) to obtain a measure of the important LOSs and the LOSs that could be used for hyper-parameter optimization (Eq. 27). For example, cases 1-7 exhibit high average radiative intensity as the corresponding LOS are close to the stagnation region. The model prediction must be good for these LOSs. In contrast, cases 8-15 exhibit negligible radiative intensities, and hence a high prediction error associated with these cases is acceptable. In other words, the LOSs that exhibit high average radiative intensities can be used to solve the optimization problem (Eq. 27). The hyper-parameters obtained by solving such an optimization problem will result in an ML model that ensures good performance across the important LOSs. Finally, the performance of the ML model across the entire set of unseen LOSs is depicted by Fig. 5(c) and Fig. 5(d).

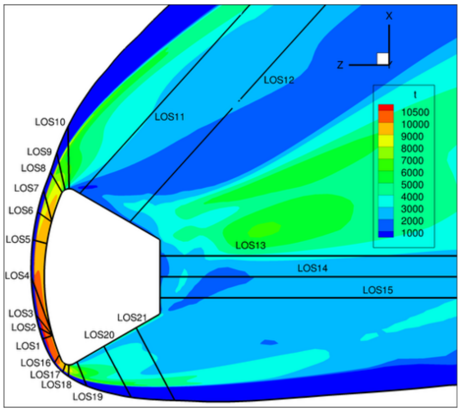

(a) Graphical representation of LOSs extracted from an Orion re-entry scenario.

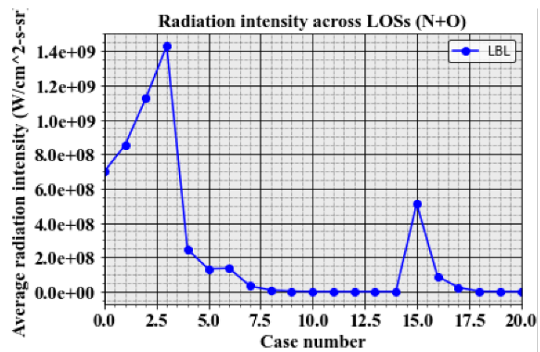

(b) Average radiative intensity across all extracted LOSs.

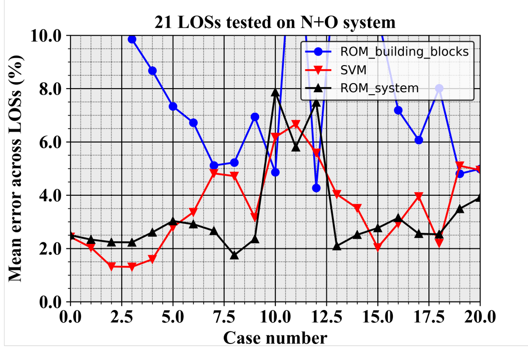

(c) Variation of mean relative error across all LOSs.

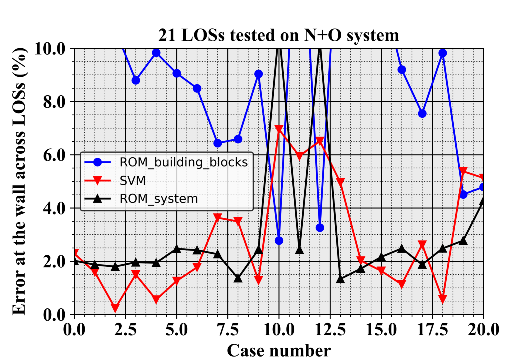

(d) Variation of relative error at the wall across all LOSs.

Fig. 5 Performance evaluation of the ML model across LOSs unseen by the model.

In Fig. 5(c), the mean relative errors observed across the LOSs with respect to the "ROM building blocks", the "ROM system" and the "SVM correction" are plotted. The ML model correction exhibits lower relative error and a trend closer to the case specific calibrated ROM model (black curve). In addition, the relative errors associated with the important LOSs (cases 1-7) are <5%. This shows the ability of the ML model to perform well on the unseen data across the entire LOS. As explained in Sec. II, the prediction of radiative intensity at the wall directly translates to the heat flux transferred to the surface of the re-entry vehicle. This is an important design parameter for the development of thermal protection systems. Hence, there is a need to evaluate the performance of the ML model specifically with respect to the wall radiative intensity. This is represented in Fig. 5(d) and one can observe the excellent performance of the ML model even with respect to the case specific calibrated ROMs ("ROM system"). From Figs. 5(c) and 5(d) we can infer that the ML model performs well across the entire 3D radiative field and at the wall, which was possible because of the additional optimization problem solved to calibrate the hyper-parameters (Eq. 27). Hence, the performance of the ML model across the unseen data is verified with its indifference to the over-fit condition.

D. Model performance with varying optical thickness

One of the main objectives of the current work is to develop a ML correction framework that predicts the radiative intensities with varying optical thickness. The dependence of the ML model on the optical thickness was modeled using the geometric length scale (δs) as an input variable and considering additional LOSs with varying grid amplification factor (Δs) for data sampling (Table 5). For example, the Orion stagnation LOS (Fig. 3) used to train the model has a non-uniform grid with a unity grid amplification factor (Δs = 1). By changing Δs, it is possible to vary the optical thickness corresponding to a specific LOS. The ML model must be trained to handle this variation in Δs, as one can see that the relative errors associated with the "ROM building block" model (Figs. 6(a) - 6(d)) steadily grow with varying optical thickness. Furthermore, even calibrated case specific ROM ("ROM system") exhibit an exponential rise in the relative errors for non-important LOS cases (8-15), as represented in Figs. 6(a) - 6(d). This can be explained by the fact that the grouping strategy [8, 9] used to resolve the spectral dimension does not take into account the changes in optical thickness as a result of discretization length (δs). Hence, the effect of changes in optical thickness must be embedded in the ML framework for robust radiative intensity predictions.

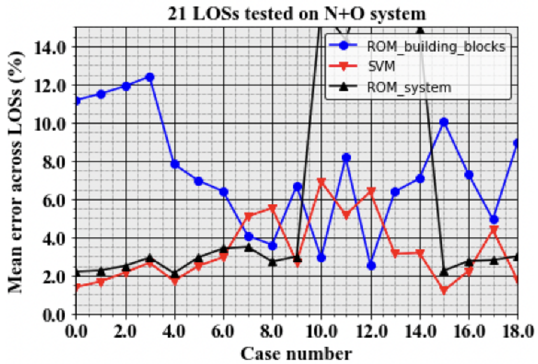

(a) Mean relative error variation across Orion LOSs (Fig. 5(a)) for a Δs = 10.

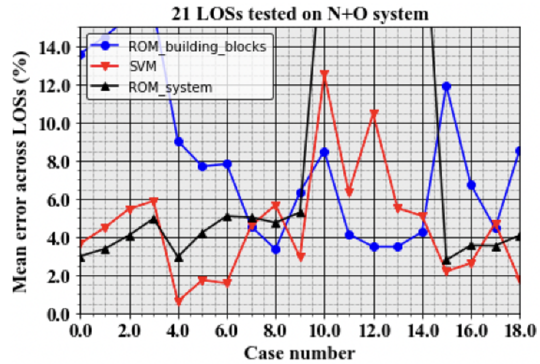

(b) Mean relative error variation across Orion LOSs (Fig. 5(a)) for a Δs = 50.

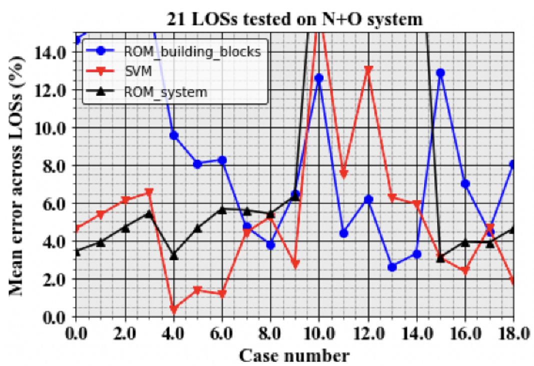

(c) Mean relative error variation across Orion LOSs (Fig. 5(a)) for a Δs = 75.

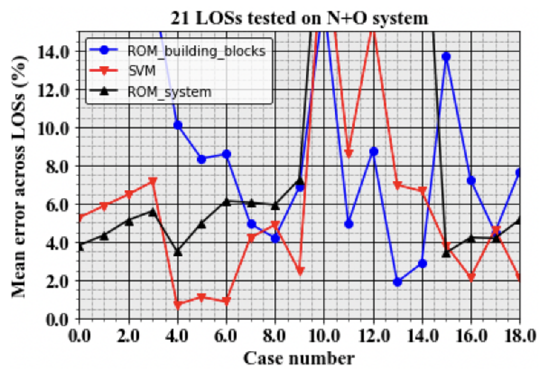

(d) Mean relative error variation across Orion LOSs (Fig. 5(a)) for a Δs = 100.

Fig. 6 Performance evaluation of the ML model with varying optical thickness.

In Figs. 6(a) - 6(d), the variation of mean relative error pertaining to the ML predictions ("SVM correction"), the "ROM building block" and the "ROM system" is plotted across all Orion LOSs with varying Δs. The mean relative error associated with "SVM correction" (red curve) in important LOS cases (1-7) is <7% and <15% for non-important LOSs (8-15). Although the mean relative errors of the "ROM system" (black curve) is closer to the "SVM correction" for LOS cases (1-7), the mean relative error of the "ROM system" is observed to grow slightly with change in optical thickness. This trend also continues across the non-important LOS cases (8-15) except with an exponential rise in error unlike the bound error observed for "SVM correction". In addition, the mean relative errors associated with the "ROM building block" model grow exponentially with a small change in optical thickness across all LOS cases. The unique bounded (<15%) nature of the error observed in the "SVM correction" for all optical thickness indicates an inherent mapping learned by the ML framework which accounts for missing physical mechanisms (exchange of photons between disparate species) prevalent at higher optical thickness. The important and non-important LOSs are categorized on the basis of the total radiation contribution from each LOS. This is consistent with the discussion presented in Fig. 5(b). Hence, from the above discussion the ability of the ML model to capture the effects of changing optical thickness on the radiative intensity is verified.

E. Verification of ML model through coupling with US3D-NERO framework

The ML model was coupled to the US3D-NERO framework as explained in Sec. III.D. Comparison of the ML enhanced US3D-NERO framework against optimized ROMs for O and N radiation ("ROM system") was performed at two different trajectory points (Figs. 7) and 8 of the Orion space capsule. The computational setup and mesh configuration remained identical for both the points of the trajectories except for the parameters directly influenced by the altitude of the said trajectories. A 3D computational grid encompassing the Orion capsule and extending just beyond the shoulder of the capsule is utilized for the subsequent analysis. The volumetric domain surrounding the capsule is discretized using hexahedral mesh elements. The freestream conditions were defined by the altitude of the capsule. The flow field around the Orion capsule was assumed to consist of an 11-species air model (N, $N+$, O, $O+$, NO, $NO+$, N_2, N_2+, O_2, O_2+ and $e-$). The chemical kinetic rate and the relaxation coefficients presented in [35] are used. Additionally, the walls of the spacecraft are assumed to be fully catalytic and in radiative equilibrium with a user defined value of emissivity. The supersonic flow boundary conditions were prescribed on the remaining boundary faces. In addition, the flow was considered to be laminar and no explicit turbulence modeling was incorporated into the results. A one-way coupling between the flow and radiation fields was considered where a steady-state flow field solution was first obtained using US3D, followed by radiative transfer calculations using NERO. The above simulation setup was implemented twice for each trajectory point, one with a normal US3D-NERO framework and one with the ML model embedded in the NERO radiative solver. The wall radiative heat flux estimated by both implementations was compared with each other by extracting a line plot along the surface of the Orion capsule (a plane defined by $y = 0$).

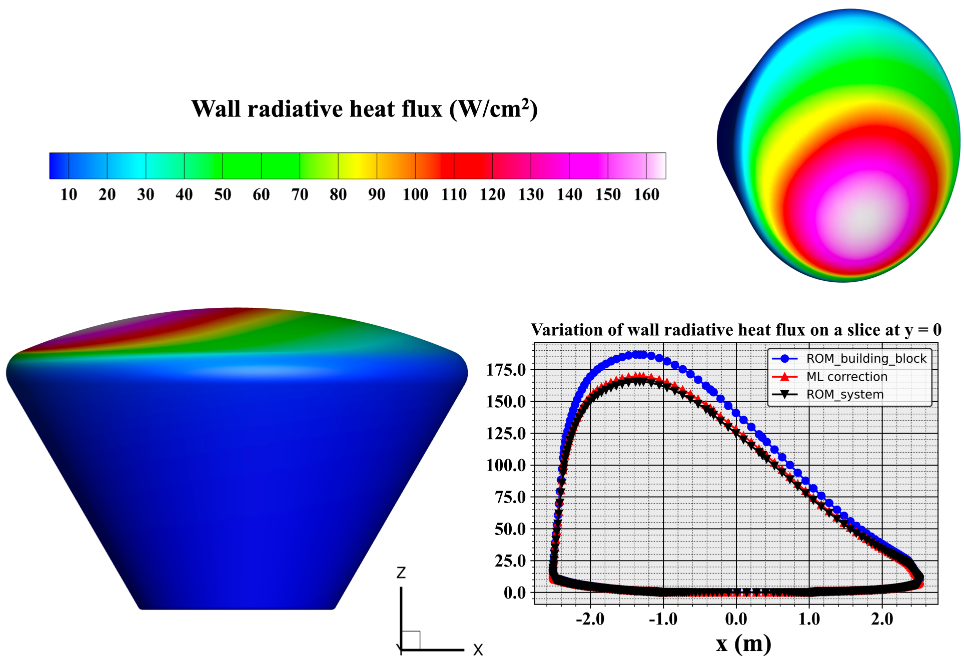

Fig. 7 Comparison of ML enhanced US3D-NERO framework with a normal US3D-NERO implementation in determining the wall radiative heat flux associated with Orion at an altitude of 10.7 km.

In Fig. 7, a contour of the wall radiative heat flux obtained by performing a one-way coupling of the US3D-NERO framework is presented at an altitude of 10.7 km. As explained in Sec.III.A, the quadrature points extracted as LOSs to obtain the 3D radiative flow field consider radiation contributions from both atomic nitrogen and oxygen. As expected, the estimated surface radiative heating at the stagnation region was significantly higher compared to other regions of the fore-body of Orion. The trends and values of surface heating agree with the peak heating lunar-return conditions [30]. The volumetric and surface radiative heating was calculated using the ROM databases which significantly reduced the computational time when compared to legacy NASA aerothermal solvers. The total computational time saved by using ROM database has been extensively studied in [8, 9]. Both a ROM database calibrated for the mixture specific application ("ROM system") and a ROM database constructed independently for each of the gas species involved ("ROM building blocks"), was compared with the ML enhanced ("ML correction") implementation of US3D-NERO framework. This is represented by the line plot extracted along the surface of the Orion capsule. Furthermore, the "ROM system" curve (black curve) is the true solution close to the fully resolved LBL method, as presented in [8, 9]. The "ROM building block" curve (blue curve) represents the radiative heat flux approximated by assuming $I_T^{ROM} = I_{\text{ROM}}(N) + I_{\text{ROM}}(O)$.

The "ML correction" curve (red curve) uses the assumptions of the "ROM building block" model to obtain the true solution.

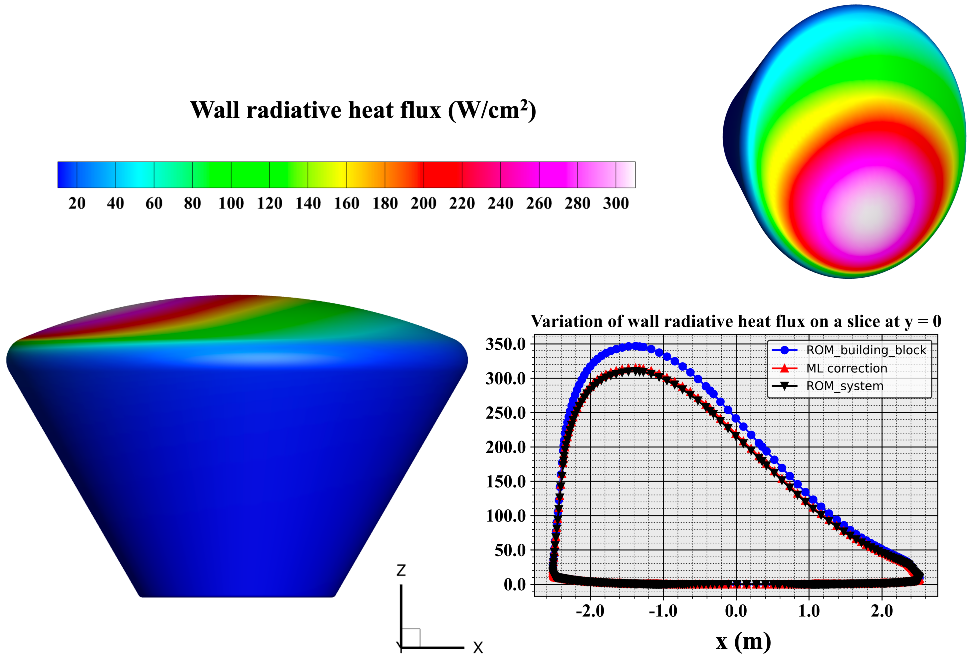

Fig. 8 Comparison of ML enhanced US3D-NERO framework with a normal US3D-NERO implementation in determining the wall radiative heat flux associated with Orion at an altitude of 10.5 km.

To prove that the ability of the ML model illustrated in Fig. 7 was not a one off aberration, a comparison of wall radiative heat flux between normal and ML enhanced US3D-NERO framework was performed at an additional trajectory point of the Orion space capsule (Fig. 8). The trends of the contour and the line plot were identical to Fig. 8. A higher peak value of radiative flux was observed at an altitude of 10.5 km as a consequence of a higher free stream velocity. The line plot in Fig. 8 again showcased the capability of the ML model to build on the assumptions of the "ROM building block" model to obtain the true solution ("ROM system"). Figures 7 and 8 point towards a powerful solution where the ML model captures the error between independently constructed ROM databases and calibrated case specific ROMs. In other words, the current ML framework could in theory be extended to a system where radiative contributions must be considered from a group of gas species without the need to re-calibrate the ROMs for each specific case (Eq. 3). Hence, the need to couple such an ML model to further enhance the US3D-NERO framework is justified.

V. Conclusion

Radiation heat transfer affects the flow field surrounding a hypersonic vehicle during re-entry conditions. The radiative heat flux transferred to the surface of re-entry vehicle also serves as a necessary design parameter to develop thermal protection systems. Hence, an efficient simulation framework is required to determine the volumetric and surface heating associated with the re-entry vehicles. Generally, the radiative heat flux is modeled as a source term in the governing equations of state-of-the-art CFD solvers. The integro-differential nature and the existence of 6 DOFs associated with the radiative heat flux ensure the need to use sophisticated radiative solvers to resolve the radiative transfer equation. Efficient radiative solvers that incorporate the Lebedev-type quadrature method for angular discretization, the finite volume method for spatial discretization, and novel radiative coefficients grouping strategies have been developed to resolve the spectral dimension. The grouping strategies developed to resolve the spectral dimension are also known as the ROMs and are constructed to hold good for non-equilibrium radiative properties that are applicable to a broad range of hypersonic re-entry scenarios. The constructed ROM databases achieve a significant increase in the rate at which radiative heat flux is evaluated with a minimal loss in accuracy (<5%), when compared to fully resolved spectral solutions (LBL method). However, the ROM databases have to re-calibrated with the inclusion of radiative contribution of additional species, as the frequency based grouping strategy needs to accommodate for the new and overlapping emission and absorption lines. In addition, the grouping strategy does not account for the variation in optical thickness as a result of the change in discretized length (δs). Hence, there is a need to develop a general purpose mathematical framework that can model the error associated with ROM based radiative transfer calculations.

In this work, the underlying problem statement was broken down into a simple 1D domain with radiation contributions from atomic oxygen and atomic nitrogen to highlight the potential of the general purpose ML framework. A correction term (F_s) was formulated for each discretized point of the 1D domain that models the error between the high fidelity LBL method and ROM approximations. Initially, F_s was assumed to depend on all the available input variables. PCA helped to capture the essential features in the sampled data, thereby reducing the dimensionality of the problem. The need for a closed form solution provided enough motivation to use the support vector regression technique to model the correction terms. The ML framework was trained on LOSs extracted from Orion, Stardust, FIRE II hypersonic re-entry scenarios. The performance of the trained model was verified by noting its indifference towards under-fit and over-fit conditions. In addition, the ability of the ML model to capture the effects of optical thickness on radiative intensity was verified. The relative errors associated with ROM approximations was seen to grow with change in optical thickness, whereas the ML model remained indifferent. This was likely a result of the use of discretized length (δs) as input variable, which is the main reason for the change in optical thickness. Finally, the need for such a general purpose ML model was verified by embedding the model into a US3D-NERO framework. The radiative heat flux at the wall for two separate Orion trajectory points predicted by the ROM approximations was compared to the ML corrected values. The ML model was shown to use independently built single species ROM databases to obtain a solution closer to calibrated case specific ROMs (multi species radiative systems). This highlighted the potential to extend the current framework to multi species radiative systems involving more than just atomic nitrogen and atomic oxygen.

Acknowledgments

We thank NASA Advanced Supercomputing (NAS) division for their support and use of the associated research computing resources. This work was supported by a Space Technology Research Institutes grant from NASA's Space Technology Research Grants Program under grant number 80NSSC21K1117. Funding support from AFOSR grant number FA9550-25-10302 and ARO cooperative agreement W911NF-25-2-0183 is also acknowledged

References

[1] Dillman, R. A., and Corliss, J. M., "Overview of the Mars Sample Return Earth Entry Vehicle," *6th International Planetary Probe Workshop*, 2008.

[2] Brandis, A. M., Saunders, D. A., Allen, G. A., Stern, E. C., Wright, M. J., Mahzari, M., Johnston, C. O., Hill, J. P., Adams, D. S., and Lorenz, R. D., "Aerothermodynamics for Dragonfly's Titan Entry," *15th International Planetary Probe Workshop*, 2018.

[3] Yoon, S., Gnoffo, P. A., White, J., and Thomas, J., "Computational challenges in hypersonic flow simulations," *39th AIAA Thermophysics Conference*, 2007. AIAA Paper 2007-4265.

[4] Brandis, A. M., Saunders, D. A., Johnston, C. O., Cruden, B. A., and White, T. R., "Radiative heating on the after-body of Martian entry vehicles," *Journal of Thermophysics and Heat Transfer*, Vol. 34, No. 1, 2020, pp. 66–77.

[5] Candler, G. V., Johnson, H. B., Nompelis, I., Gidzak, V. M., Subbareddy, P. K., and Barnhardt, M., "Development of the US3D code for advanced compressible and reacting flow simulations," *AIAA Paper 2015-1893*, 2015.

[6] Lamet, J.-M., Babou, Y., Riviere, P., Perrin, M.-Y., and Soufiani, A., "Radiative transfer in gases under thermal and chemical nonequilibrium conditions: Application to Earth atmospheric re-entry," *Journal of Quantitative Spectroscopy and Radiative Transfer*, Vol. 109, No. 2, 2008, pp. 235–244.

[7] Brewster, M. Q., *Thermal Radiative Transfer and Properties*, John Wiley & Sons, 1992.

[8] Sahai, A., and Johnston, C. O., "On Computationally Efficient Radiative Transfer Calculations for Three-dimensional Entry Problems," *AIAA SCITECH 2023 Forum*, 2023. https://doi.org/10.2514/6.2023-0204, URL https://arc.aiaa.org/doi/abs/10.2514/6.2023-0204.

[9] Sahai, A., and Johnston, C., "Generalized reduced-order spectral models for non-equilibrium radiative transfer in complex hypersonic entry environments," *Journal of Quantitative Spectroscopy and Radiative Transfer*, 2026. Under review.

[10] Johnston, C. O., Sahai, A., and Panesi, M., "Extension of Multiband Opacity-Binning to Molecular, Non-Boltzmann Shock Layer Radiation," *Journal of Thermophysics and Heat Transfer*, 2017, pp. 1–6.

[11] Sahai, A., Johnston, C. O., Lopez, B., and Panesi, M., "Comparative analysis of reduced-order spectral models and grouping strategies for non-equilibrium radiation," *Journal of Quantitative Spectroscopy and Radiative Transfer*, Vol. 242, 2020, p. 106752.

[12] Keane, A., Forrester, A., and Sobester, A., *Engineering Design via Surrogate Modelling: A Practical Guide*, 2008. https://doi.org/10.2514/4.479557.

[13] Baldi, P., and Hornik, K., "Neural networks and principal components analysis: learning from examples without local minima," *Neural Networks*, Vol. 2, No. 1, 1989, pp. 53–58.

[14] Baron, E., "Spectral Modeling of Type II Supernovae," *AIP Conference Proceedings*, Vol. 924, 2007, pp. 350–357. https://doi.org/10.1063/1.2774880.

[15] Scherding, C., Rigas, G., Sipp, D., Schmid, P. J., and Sayadi, T., "Data-driven framework for input/output lookup tables reduction: Application to hypersonic flows in chemical nonequilibrium," *Physical Review Fluids*, Vol. 8, No. 2, 2023, p. 023201.

[16] Kopparla, P., Natraj, V., Spurr, R., Shia, R.-L., Crisp, D., and Yung, Y. L., "A fast and accurate PCA based radiative transfer model: Extension to the broadband shortwave region," *Journal of Quantitative Spectroscopy and Radiative Transfer*, Vol. 173, 2016, pp. 65–71. https://doi.org/https://doi.org/10.1016/j.jqsrt.2016.01.014, URL https://www.sciencedirect.com/science/article/pii/S0022407315300662.

[17] Bellemans, A., Munafò, A., Magin, T. E., Degrez, G., and Parente, A., "Reduction of a collisional-radiative mechanism for argon plasma based on principal component analysis," *Physics of Plasmas*, Vol. 22, No. 6, 2015, p. 062108. https://doi.org/10.1063/1.4922077, URL https://doi.org/10.1063/1.4922077.

[18] Vapnik, V. N., *The Nature of Statistical Learning Theory*, Springer, 1995. https://doi.org/10.1007/978-1-4757-2440-0.

[19] Alamaniotis, M., Mattingly, J., and Tsoukalas, L., "Kernel-Based Machine Learning for Background Estimation of NaI Low-Count Gamma-Ray Spectra," *IEEE Transactions on Nuclear Science*, Vol. 60, No. 3, 2013, pp. 2209–2221. https://doi.org/10.1109/TNS.2013.2260868.

[20] Prado, D. R., López-Fernández, J. A., and Arrebola, M., "Systematic Study of the Influence of the Angle of Incidence Discretization in Reflectarray Analysis to Improve Support Vector Regression Surrogate Models," *Electronics*, Vol. 9, No. 12, 2020. https://doi.org/10.3390/electronics9122105, URL https://www.mdpi.com/2079-9292/9/12/2105.

[21] Camporeale, E., Wilkie, G. J., Drozdov, A. Y., and Bortnik, J., "Data-Driven Discovery of Fokker-Planck Equation for the Earth's Radiation Belts Electrons Using Physics-Informed Neural Networks," *Journal of Geophysical Research: Space Physics*, Vol. 127, No. 7, 2022, p. e2022JA030377. https://doi.org/https://doi.org/10.1029/2022JA030377, URL https://agupubs.onlinelibrary.wiley.com/doi/abs/10.1029/2022JA030377, e2022JA030377 2022JA030377.

[22] Johnston, C. O., "Nonequilibrium shock-layer radiative heating for Earth and Titan entry," Ph.D. thesis, Virginia Polytechnic Institute and State University, 2006.

[23] Mazaheri, A., Gnoffo, P. A., Johnston, C. O., and Kleb, B., "LAURA Users Manual: 5.5-65135," Tech. rep., NASA TM 2013-217800, 2013.

[24] Johnston, C., and Panesi, M., "Advancements in afterbody radiative heating simulations for Earth entry," *46th AIAA Thermophysics Conference*, 2016. AIAA Paper 2016-3693.

[25] Guyon, I., and Elisseeff, A., "An introduction to variable and feature selection," *Journal of Machine Learning Research*, Vol. 3, 2003, pp. 1157–1182.

[26] Jolliffe, I. T., and Cadima, J., "Principal component analysis: A review and recent developments," *Philosophical Transactions of the Royal Society A*, Vol. 374, No. 2065, 2016.

[27] Hotelling, H., "Analysis of a complex of statistical variables into principal components," *Journal of Educational Psychology*, Vol. 24, 1933, pp. 417–441.

[28] Smola, A. J., and Schölkopf, B., "A tutorial on support vector regression," *Statistics and Computing*, Vol. 14, No. 3, 2004, pp. 199–222. https://doi.org/https://doi.org/10.1023/B:STCO.0000035301.49549.88.

[29] Cristianini, N., and Shawe-Taylor, J., *An introduction to support vector machines and other kernel-based learning methods*, Cambridge University Press, 2000. https://doi.org/https://doi.org/10.1017/CBO9780511801389.

[30] Kleb, B., and Johnston, C. O., "Uncertainty analysis of air radiation for Lunar return shock layers," *AIAA Atmospheric Flight Mechanics Conference and Exhibit*, 2008. AIAA Paper 2008-6388.

[31] Johnston, C. O., and Panesi, M., "Impact of state-specific flowfield modeling on atomic nitrogen radiation," *Physical Review Fluids*, Vol. 3, No. 1, 2018, p. 013402.

[32] Johnston, C. O., and Brandis, A. M., "Features of afterbody radiative heating for earth entry," *Journal of Spacecraft and Rockets*, Vol. 52, No. 1, 2015, pp. 105–119.

[33] Afzal, A., Kim, K. Y., and Seo, J. W., "Effects of latin hypercube sampling on surrogate modeling and optimization," *International Journal of Fluid Machinery and Systems*, 2017. https://doi.org/10.5293/IJFMS.2017.10.3.240.

[34] Pedregosa, F., Varoquaux, G., Gramfort, A., Michel, V., Thirion, B., Grisel, O., Blondel, M., Prettenhofer, P., Weiss, R., Dubourg, V., Vanderplas, J., Joly, A., Passos, D., Cournapeau, D., Perrot, M., and Duchesnay, E., "Scikit-learn: Machine Learning in Python," *Journal of Machine Learning Research*, Vol. 12, 2011, pp. 2825–2830.

[35] Park, C., "Review of chemical-kinetic problems of future NASA missions. I—Earth entries," *Journal of Thermophysics and Heat Transfer*, Vol. 7, No. 3, 1993, pp. 385–398.